Available online at www.sciencedirect.com
ScienceDirect
Journal of Sound and Vibration 314 (2008) 507–525
JOURNAL OF SOUND AND VIBRATION
www.elsevier.com/locate/jsvi

Concurrent mechatronic design approach for active control of cavity noise

L.P.R. de Oliveira*, M.M. da Silva, P. Sas, H. Van Brussel, W. Desmet

Department of Mechanical Engineering, Katholieke Universiteit Leuven, Celestijnenlaan 300 B, B-3001, Leuven, Belgium

Received 28 July 2007; received in revised form 26 October 2007; accepted 2 January 2008
Handling Editor: C. Morfey
Available online 15 February 2008

Abstract

Active control is a potential solution to many noise and vibration problems for improving the low-frequency performance. Cavity noise reduction as encountered for instance in aircraft cabins and vehicle interiors is a typical example. However, the conventional design of these active solutions may lead to suboptimal products, since the interaction between the vibro-acoustic plant dynamics and control dynamics is usually not considered. A proper way to design such active systems would be considering control and plant parameters concurrently. To cope with this approach, a methodology to derive a fully coupled mechatronic model that deals with both the vibro-acoustic plant dynamics as well as the control parameters is proposed. The inclusion of sensor and actuator models is investigated, since it contributes to the model accuracy as it can confer frequency, phase or amplitude limitations to the control performance. The proposed methodology provides a reduced state-space model derived from a fully coupled vibro-acoustic finite element model. Experimental data on a vibro-acoustic vehicle cabin mock-up are used to validate the model reduction procedure. Regarding noise reduction, optimization results are presented considering both vibro-acoustic plant features, such as thicknesses, and control parameters, such as sensor and actuator placement and control gains. A collocated sensor/actuator pair is considered in a velocity feedback control strategy. The benefits of a concurrent mechatronic design when dealing with active structural–acoustic control solutions are addressed, illustrated and experimentally validated.

1. Introduction

The demands for improvement in sound quality and reduction of noise generated by vehicles, as well as the penalties for space and weight of passive solutions are steadily increasing. Active solutions have the potential to enhance the dynamic performance beyond the passive performance which may allow a lighter and improved product [1].

Demonstrations of the viability of active noise control (ANC) and active structural–acoustic control (ASAC) in cavity noise applications, including automotive interior noise reduction, have been described by several authors [1–6]. A relatively new development in ASAC is the use of decentralized controllers,

*Corresponding author. Tel.: +32 16 32 24 80; fax: +32 16 32 29 87.
E-mail address: leopoldo.deoliveira@mech.kuleuven.be (L.P.R. de Oliveira).

0022-460X/$ - see front matter © 2008 Elsevier Ltd. All rights reserved.
doi:10.1016/j.jsv.2008.01.009

i.e., systems with sensors and actuators connected as independent pairs in feedback loops, rather than through a centralized control unit. This technique has received considerable attention [7–11], mainly because of its advantages over the centralized strategy in terms of the practical realization (simpler connections and savings on cabling) and the system transducer fault tolerance [11]. The importance of the proper placement of sensors and actuators has also been highlighted in Refs. [9,11–13].

Nowadays, virtual prototyping techniques are being developed in order to support the design process and to improve product performance, while reducing design costs and shortening development cycles [14]. In order to bring active solutions to the level of industrial applications, the designer needs numerical tools that allow the inclusion of sensors/actuators and control strategy in the virtual product design and optimization. In this way, the design of active solutions for noise reduction should be performed along the lines of a mechatronic design approach. For the purpose of this study, a mechatronic design is defined as an approach that deals with the integrated design of a mechanical system and its embedded control system [15]. This approach has been illustrated by performing a concurrent optimization for a 3-axis machine tool considering control and structural aspects, resulting in an improved system performance [16]. For active noise control, the concurrent mechatronic approach has been rarely employed. Recently, a simultaneous structural and control optimization of a flexible linkage mechanism for noise attenuation has been described [17]. In that case, the aim is to reduce the structural–acoustic radiation of a flexible mechanism considering in the objective function the weight of the structure, the vibration energy and the control system energy. It is claimed that the integrated approach improved significantly the acoustic radiation (performance) and the controller inputs (effort) for that case study.

In this paper, a concurrent mechatronic approach to active control design for interior cavity noise reduction, as encountered for instance in automotive interior applications, is proposed using simulation and optimization. The benefits of this methodology are demonstrated on a vibro-acoustic cabin mock-up (Figs. 1 and 2). It consists of a simplified car cavity with concrete walls to provide well-defined acoustic boundary conditions, thus reducing uncertainties during the vibro-acoustic modeling phase. The system is divided into two closed cavities: the passenger compartment (PC) and the engine compartment (EC). A rectangular clamped steel panel resembles the firewall, allowing the disturbance noise generated by the acoustic source in the EC to be transmitted to the PC. The PC main dimensions are $3400 \times 1560 \times 1270\,\mathrm{mm}^3$; the EC is $800 \times 1100 \times 750\,\mathrm{mm}^3$; and the firewall is $895 \times 545 \times 1.5\,\mathrm{mm}^3$ (Fig. 2). A structural sensor/actuator pair (SAP) placed on the firewall realizes the control signals for noise reduction in the PC.

One of the challenges lies in deriving reasonably sized models that integrate the structural, acoustic and electrical components along with the control algorithm. Moreover, the presence of distinct paths (fluid–structure–fluid) imposes the necessity of dealing with fully coupled vibro-acoustic models. In order to fulfill this requirement, a fully coupled finite element (FE) model of the vibro-acoustic system is reduced and exported as a state-space (SS) model into Matlab/Simulink. The inclusion of sensor and actuator models, which can be realized in this environment, contributes to the model accuracy, since their own dynamics may change the original system response significantly.

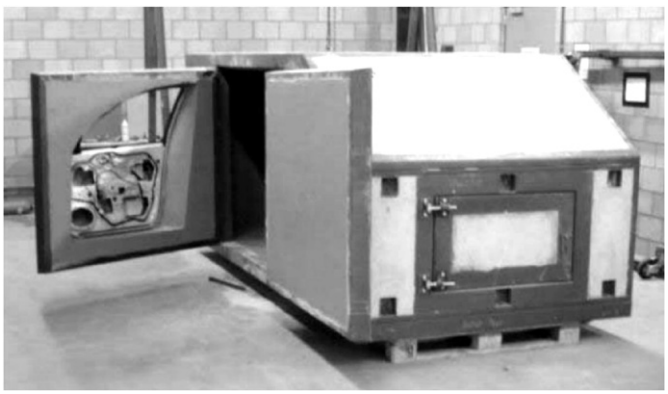

Fig. 1. Photo of the experimental setup: the vibro-acoustic cabin mock-up.

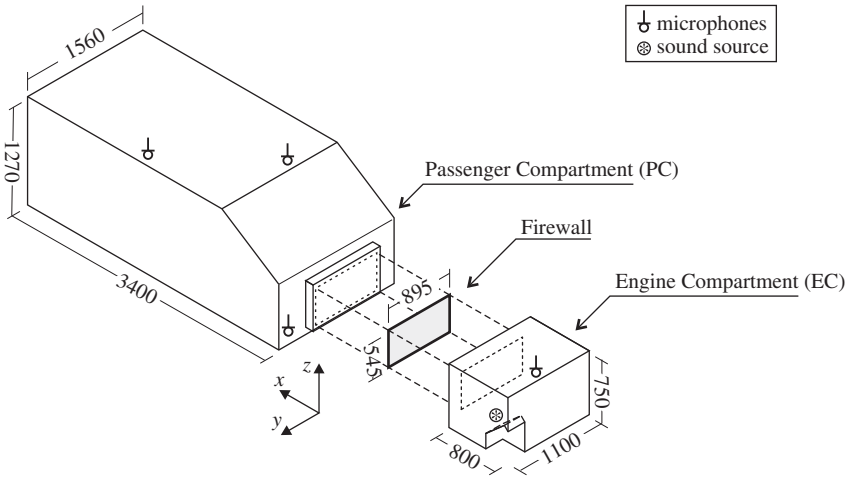

Fig. 2. Schematic view of the system under study (dimensions in mm).

The modeling approach for the fully coupled vibro-acoustic system and its experimental validation are presented in Section 2. The integrated design of the active system is treated in Section 3. Finally, some conclusions are addressed in Section 4.

2. Fully coupled vibro-acoustic modeling approach

Vibro-acoustic systems can be modeled using Computer Aided Engineering (CAE) tools such as FE and/or boundary element (BE) methods. In order to improve the prediction of the structural behavior in the presence of fluid loads, simulation procedures have been proposed [18–20], where the influence of the fluid (modeled with BE) is included in the original structural FE models. The present case study, however, requires not only the fluid load on the structure but also the interaction between the structural vibrations and the pressure field. In other words, the vibro-acoustic model should be fully coupled. To cope with this, a coupled vibro-acoustic FE/FE modeling approach is adopted [21]. As a result, any combination of structural and acoustic inputs/outputs can be used for the control design, e.g., an acoustic source in the EC, structural sensors and actuators on the firewall and a microphone in the PC.

Another advantage of using a fully coupled vibro-acoustic approach is the accuracy of the estimated closed-loop performance, as an uncoupled analysis can overestimate the controller efficiency [22]. It is also required that the modeling approach fits into an optimization loop, as the design of an active control system usually requires the setting of some controller parameters (e.g. sensor and actuator positions and control gains).

One of the coupled FE/FE formulations is the Eulerian, in which the structural degrees of freedom (dofs) are displacement vectors, while the acoustic dofs are expressed as scalar functions. The latter is usually the acoustic pressure, but can also be the fluid velocity potential [23–27]. If pressure is adopted, the system of equations yields non-symmetrical mass and stiffness matrices, posing a disadvantage to FE solvers. The choice of velocity potential as acoustic dof also presents a drawback, as the vibro-acoustic coupling terms populate the damping matrix, yielding a symmetric but complex model, which is computationally more expensive than the non-symmetric one [28]. Moreover, the modal base resulting from the non-symmetric eigenproblem can easily be handled by the modeling procedure, as will be described in more detail in the next section. Therefore, a displacement/pressure Eulerian formulation is adopted hereafter.

2.1. From vibro-acoustic FE to state-space formulation

Usually, control design and simulation is performed in a dedicated time-domain environment, raising the necessity of deriving a compatible representation of the system under study. An appropriate approach would be a modal representation of the FE model in a SS formulation. This representation is a mathematical model

of a physical system as a set of input, output and state variables related by first-order differential equations, providing a convenient and compact way to model and analyze systems with multiple inputs and outputs. A number of control design tools are available for systems described in this form such as linear-quadratic-Gaussian (LQG) design, linear-quadratic state-feedback regulator design (LQR) and H_∞ controller synthesis. The purpose of this paper is to deliver tools to allow the designer to perform a concurrent mechatronic design; therefore, the SS representation suits this objective better.

A first step in the FE modeling of vibro-acoustic systems is the definition of appropriate meshes for the acoustic and structural components. Coincident structural and acoustic meshes are adopted over the coupling boundary resulting in a simplified procedure [29]. The frequency range of interest is limited to 0–200 Hz to reduce the computational effort during the modeling procedure. It may not be representative for all interior acoustic problems, but is sufficient to demonstrate the proposed technique and to provide general insights. Moreover, this choice is not a limiting factor, since this technique is valid as far as FE models can be used.

The size of the structural elements is chosen such that the highest-order mode (at 160 Hz: see Fig. 3b and Table 1) is represented by at least 6 linear elements. The structural mesh (Fig. 3a) has 200 4-noded shell elements, yielding 1026 dofs since the borders of the firewall are clamped. The chosen 4-node shell element was an isoparametric quadrilateral element with the evaluation of the forces at the centroid of the element (QUAD4). This element may exhibit locking effects for trapezoidal shapes [30]. Due to the characteristic of the geometry, a rectangular mesh was employed avoiding this phenomenon. Experimental validation, showed hereafter, confirms the model accuracy. However, the locking phenomenon should be addressed properly when more complicated geometries and meshes are involved. The 1.5 mm-thick firewall presents 12 modes between 0 and 200 Hz (Table 1).

The element type chosen for the acoustic mesh is the 8-noded brick element. The resulting mesh, with 26,050 elements, and the mode shape at 192.5 Hz are depicted in Fig. 4. The total number of acoustic dofs is 23,196. With respect to the element size, this acoustic model exhibits a minimum of 6 linear elements per wavelength up to 500 Hz.

Table 1 shows the resonance frequencies for the coupled vibro-acoustic model and the uncoupled structural and acoustic components. It also shows the mode shapes in terms of the number of half-wavelengths in the x, y and z directions for the uncoupled modes.

In a coupled FE/FE approach, the effect of the fluid on the structure dynamics can be considered as a pressure load on the wetted surface. For a system with n_s structural dofs and n_a acoustic dofs, the structural differential equation takes the form of Eq. (1).

$$(\mathbf{K}_s + \mathrm{j}\omega\mathbf{D}_s - \omega^2\mathbf{M}_s)\mathbf{u}(\omega) + \mathbf{K}_c\mathbf{p}(\omega) = \mathbf{F}_s(\omega), \tag{1}$$

where $\mathbf{K}_s$, $\mathbf{D}_s$ and $\mathbf{M}_s \in \mathbb{R}^{n_s \times n_s}$ are, respectively, the stiffness, damping and mass matrices of the structural component, $\mathbf{K}_c \in \mathbb{R}^{n_s \times n_a}$ is the coupling matrix, $\mathbf{u} \in \mathbb{R}^{n_s \times 1}$ is the vector of structural displacement dofs, $\mathbf{p} \in \mathbb{R}^{n_a \times 1}$ is the vector of nodal acoustic pressures and $\mathbf{F}_s \in \mathbb{R}^{n_s \times 1}$ is the structural load vector.

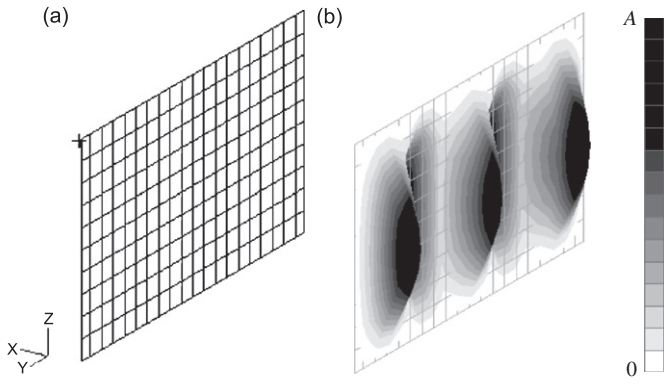

Fig. 3. Firewall: (a) FE mesh and (b) uncoupled mode at 160 Hz [5,1].

Table 1
Resonance frequencies for coupled and uncoupled systems

Vibro-acoustic modes		Uncoupled structural modes		Uncoupled acoustic modes	
Modes #	Freq. (Hz)	Freq. (Hz)	Half-wavelength (y,z)	Freq. (Hz)	Wavelength (x,y,z)
1	0			0	EC - [0,0,0][a]
2	0			0	PC - [0,0,0][b]
3	35.3	34.2	[1,1]		
4	49.1	48.3	[2,1]		
5	52.5			52.1	PC - [1,0,0]
6	75.6	75.6	[3,1]		
7	85.9	86.0	[1,2]		
8	99.4	99.4	[2,2]		
9	101.8			101.6	PC - [2,0,0]
10	110.5			110.6	PC - [0,1,0]
11	112.5	112.6	[4,1]		
12	122.4	122.5	[3,2]		
13	122.9			122.8	PC - [1,1,0]
14	137.2			137.2	PC - [0,0,1]
15	145.9			145.9	PC - [3,0,0]
16	151.3			151.3	PC - [2,1,0]
17	155.7	155.7	[4,2]		
18	157.1			157.2	PC - [1,0,1]
19	159.0			158.7	EC - [0,1,0]
20	160.0	159.9	[5,1][c]		
21	164.5	164.5	[1,3]		
22	176.0			176.0	PC - [0,1,1]
23	177.8	177.8	[2,3]		
24	182.9			182.8	PC - [2,0,1]
25	184.1			184.1	PC - [1,1,1]
26	192.5			192.5	PC - [2,1,1][d]
27	198.9	199.0	[3,3]		
28	199.4			199.7	PC - [4,0,0]

[a]EC = Engine compartment.
[b]PC = Passenger compartment.
[c]Mode depicted in Fig. 3.
[d]Mode depicted in Fig. 4.

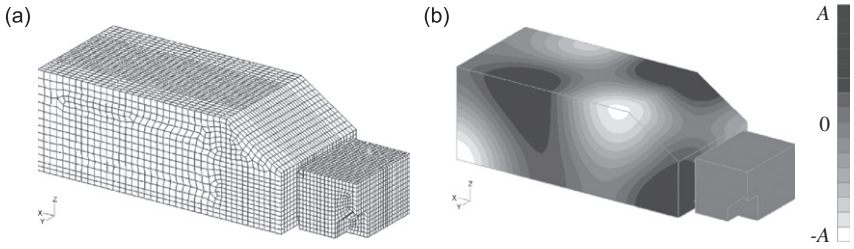

Fig. 4. Acoustic cavities: (a) FE mesh and (b) uncoupled mode at 192.5 Hz.

In a similar way, the structural vibrations provide an acoustic velocity input and therefore must be taken into account in the acoustic model as

$$(\mathbf{K}_a + \mathrm{j}\omega\mathbf{D}_a - \omega^2\mathbf{M}_a)\mathbf{p}(\omega) + \omega^2\mathbf{M}_c\mathbf{u}(\omega) = \mathbf{F}_a(\omega), \tag{2}$$

where $\mathbf{K}_a$, $\mathbf{D}_a$ and $\mathbf{M}_a \in \mathbb{R}^{n_a \times n_a}$ are the acoustic stiffness, damping and mass matrices, $\mathbf{M}_c \in \mathbb{R}^{n_a \times n_s}$ is the coupling matrix and $\mathbf{F}_a \in \mathbb{R}^{n_a \times 1}$ is the acoustic load vector. For the sake of brevity, any frequency-dependent function '$h(\omega)$' is represented just as 'h' hereafter.

Using the relation $\mathbf{M}_c = -\rho_0 \mathbf{K}_c^{\mathrm{T}}$ [31–34], where $\boldsymbol{\rho}_0$ is the fluid density, the combined system of equations, known as the Eulerian FE/FE model, yields:

$$\left(\begin{bmatrix} \mathbf{K}_s & \mathbf{K}_c \\ \mathbf{0} & \mathbf{K}_a \end{bmatrix} + \mathrm{j}\omega \begin{bmatrix} \mathbf{D}_s & \mathbf{0} \\ \mathbf{0} & \mathbf{D}_a \end{bmatrix} - \omega^2 \begin{bmatrix} \mathbf{M}_s & \mathbf{0} \\ -\rho_0 \mathbf{K}_c^{\mathrm{T}} & \mathbf{M}_a \end{bmatrix} \right) \begin{Bmatrix} \mathbf{u} \\ \mathbf{p} \end{Bmatrix} = \begin{Bmatrix} \mathbf{F}_s \\ \mathbf{F}_a \end{Bmatrix}. \tag{3}$$

Based on Eq. (3) it is clear that the resulting vibro-acoustic system is coupled, though it is no longer symmetric. As a consequence of this non-symmetric nature, the solution of the associated undamped eigenproblem is computationally more demanding and results in different left and right eigenvectors:

$$\begin{bmatrix} \mathbf{K}_s & \mathbf{K}_c \\ \mathbf{0} & \mathbf{K}_a \end{bmatrix} \{\boldsymbol{\Phi}_R\}_r = \omega_r^2 \begin{bmatrix} \mathbf{M}_s & \mathbf{0} \\ -\rho_0 \mathbf{K}_c^{\mathrm{T}} & \mathbf{M}_a \end{bmatrix} \{\boldsymbol{\Phi}_R\}_r, \quad r = 1, \ldots, n_a + n_s, \tag{4}$$

$$\{\boldsymbol{\Phi}_L\}_r^{\mathrm{T}} \begin{bmatrix} \mathbf{K}_s & \mathbf{K}_c \\ \mathbf{0} & \mathbf{K}_a \end{bmatrix} = \omega_r^2 \{\boldsymbol{\Phi}_L\}_r^{\mathrm{T}} \begin{bmatrix} \mathbf{M}_s & \mathbf{0} \\ -\rho_0 \mathbf{K}_c^{\mathrm{T}} & \mathbf{M}_a \end{bmatrix}, \quad r = 1, \ldots, n_a + n_s, \tag{5}$$

where r is the index of the coupled natural frequency ω_r and $\boldsymbol{\Phi}_L$ and $\boldsymbol{\Phi}_R \in \mathbb{R}^{(n_s+n_a)\times 1}$ are, respectively, the left and right coupled modes.

Moreover, it has been indicated [35] that, for the Eulerian formulation, the left and right eigenvectors can be related as

$$\{\boldsymbol{\Phi}_L\}_r = \begin{Bmatrix} \{\boldsymbol{\Phi}_{Ls}\}_r \\ \{\boldsymbol{\Phi}_{La}\}_r \end{Bmatrix} = \begin{Bmatrix} \{\boldsymbol{\Phi}_{Rs}\}_r \omega_r^2 \\ \{\boldsymbol{\Phi}_{Ra}\}_r \end{Bmatrix}, \quad r = 1, 2, \ldots, n_s + n_a, \tag{6}$$

where the indexes a and s represent, respectively, the acoustic and structural dofs.

A common practice in solving such vibro-acoustic problems is the use of component mode synthesis (CMS). It consists of expanding the structural dofs in terms of a set of N_s uncoupled structural modes $\boldsymbol{\Phi}_s \in \mathbb{R}^{n_s \times 1}$ (without any acoustic pressure load along the coupling interface), as well as expanding the acoustic dofs in terms of a set of N_a uncoupled acoustic modes $\boldsymbol{\Phi}_a \in \mathbb{R}^{n_a \times 1}$ (acoustic boundaries considered rigid at the wetted surface). The structural and acoustic expansions become, respectively,

$$\mathbf{u} = \sum_{r=1}^{N_s} q_{s_r} \{\boldsymbol{\Phi}_s\}_r = \boldsymbol{\Phi}_s \mathbf{q}_s, \tag{7}$$

$$\mathbf{p} = \sum_{r=1}^{N_a} q_{a_r} \{\boldsymbol{\Phi}_a\}_r = \boldsymbol{\Phi}_a \mathbf{q}_a, \tag{8}$$

where $\mathbf{q}_s \in \mathbb{R}^{N_s \times 1}$ is the vector of modal amplitudes related to the structural dofs, $\mathbf{q}_a \in \mathbb{R}^{N_a \times 1}$ is the vector of modal amplitudes related to the acoustic dofs, $\boldsymbol{\Phi}_s \in \mathbb{R}^{n_s \times N_s}$ is the structural modal matrix, $\boldsymbol{\Phi}_a \in \mathbb{R}^{n_a \times N_a}$ is the acoustic modal matrix and r is the index representing the number of the mode.

This procedure yields non-symmetrical coupled modal stiffness and mass matrices [34]. Therefore, obtaining the modal SS representation of a reduced model derived from CMS can be a difficult task, since it is necessary to invert the coupled modal mass matrix (which is non-diagonal) and the coupling matrix should be fully available. An alternative to describe a modal SS for a fully coupled vibro-acoustic system is to apply a variable substitution to the coupled eigenproblem related to Eq. (3) [36]. This procedure is detailed hereafter.

Substituting the component mode expansions in Eqs. (7) and (8) into Eq. (3) and pre-multiplying the structural and acoustic parts of the resulting matrix equation, respectively, with the transpose of the structural and acoustic modal vectors yields the undamped modal representation:

$$\left(\begin{bmatrix} \boldsymbol{\Phi}_s^{\mathrm{T}} \mathbf{K}_s \boldsymbol{\Phi}_s & \boldsymbol{\Phi}_s^{\mathrm{T}} \mathbf{K}_c \boldsymbol{\Phi}_a \\ \mathbf{0} & \boldsymbol{\Phi}_a^{\mathrm{T}} \mathbf{K}_a \boldsymbol{\Phi}_a \end{bmatrix} - \omega^2 \begin{bmatrix} \boldsymbol{\Phi}_s^{\mathrm{T}} \mathbf{M}_s \boldsymbol{\Phi}_s & \mathbf{0} \\ -\rho_0 \boldsymbol{\Phi}_a^{\mathrm{T}} \mathbf{K}_c^{\mathrm{T}} \boldsymbol{\Phi}_s & \boldsymbol{\Phi}_a^{\mathrm{T}} \mathbf{M}_a \boldsymbol{\Phi}_a \end{bmatrix} \right) \begin{Bmatrix} \mathbf{q}_s \\ \mathbf{q}_a \end{Bmatrix} = \begin{Bmatrix} \boldsymbol{\Phi}_s^{\mathrm{T}} \mathbf{F}_s \\ \boldsymbol{\Phi}_a^{\mathrm{T}} \mathbf{F}_a \end{Bmatrix}. \tag{9}$$

The homogeneous system of equations related to Eq. (9) can be written as

$$\begin{bmatrix} \boldsymbol{\Phi}_s^{\mathrm{T}}(\mathbf{K}_s - \omega^2\mathbf{M}_s)\boldsymbol{\Phi}_s & \boldsymbol{\Phi}_s^{\mathrm{T}}\mathbf{K}_c\boldsymbol{\Phi}_a \\ \omega^2\boldsymbol{\Phi}_a^{\mathrm{T}}\mathbf{K}_c^{\mathrm{T}}\boldsymbol{\Phi}_s & -\dfrac{1}{\rho_0}\,\boldsymbol{\Phi}_a^{\mathrm{T}}(\mathbf{K}_a - \omega^2\mathbf{M}_a)\boldsymbol{\Phi}_a \end{bmatrix} \begin{Bmatrix} \mathbf{q}_s \\ \mathbf{q}_a \end{Bmatrix} = \begin{Bmatrix} \mathbf{0} \\ \mathbf{0} \end{Bmatrix}. \tag{10}$$

Since each uncoupled mode is normalized with respect to the uncoupled mass matrices, Eq. (10) yields:

$$\begin{bmatrix} \boldsymbol{\Omega}_s^2 - \omega^2\mathbf{I} & \boldsymbol{\Phi}_s^{\mathrm{T}}\mathbf{K}_c\boldsymbol{\Phi}_a \\ \omega^2\boldsymbol{\Phi}_a^{\mathrm{T}}\mathbf{K}_c^{\mathrm{T}}\boldsymbol{\Phi}_s & -\dfrac{1}{\rho_0}\,(\boldsymbol{\Omega}_a^2 - \omega^2\mathbf{I}) \end{bmatrix} \begin{Bmatrix} \mathbf{q}_s \\ \mathbf{q}_a \end{Bmatrix} = \begin{Bmatrix} \mathbf{0} \\ \mathbf{0} \end{Bmatrix}, \tag{11}$$

where $\boldsymbol{\Omega}_s \in \mathbb{R}^{N_s \times N_s}$ and $\boldsymbol{\Omega}_a \in \mathbb{R}^{N_a \times N_a}$ are, respectively, the structural and acoustic diagonal matrices of uncoupled natural frequencies.

Eq. (11) still results in a non-symmetric eigenproblem and is therefore expensive to solve. The first line of Eq. (11) leads to

$$\mathbf{q}_s = \omega^2(\boldsymbol{\Omega}_s^2)^{-1}\mathbf{q}_s - (\boldsymbol{\Omega}_s^2)^{-1}\boldsymbol{\Phi}_s^{\mathrm{T}}\mathbf{K}_c\boldsymbol{\Phi}_a\mathbf{q}_a. \tag{12}$$

Applying the substitution $\bar{\mathbf{q}}_s = \omega^2\mathbf{q}_s$ in Eq. (12) yields:

$$\begin{Bmatrix} \mathbf{q}_s \\ \mathbf{q}_a \end{Bmatrix} = \begin{bmatrix} (\boldsymbol{\Omega}_s^2)^{-1} & -(\boldsymbol{\Omega}_s^2)^{-1}\boldsymbol{\Phi}_s^{\mathrm{T}}\mathbf{K}_c\boldsymbol{\Phi}_a \\ \mathbf{0} & \mathbf{I} \end{bmatrix} \begin{Bmatrix} \bar{\mathbf{q}}_s \\ \mathbf{q}_a \end{Bmatrix}. \tag{13}$$

Using Eq. (13) it is possible to rewrite Eq. (11) as a symmetric system of equations in $\{\bar{\mathbf{q}}_s \;\; \mathbf{q}_a\}^{\mathrm{T}}$:

$$\begin{bmatrix} \mathbf{I} - \omega^2(\boldsymbol{\Omega}_s^2)^{-1} & \omega^2(\boldsymbol{\Omega}_s^2)^{-1}\boldsymbol{\Phi}_s^{\mathrm{T}}\mathbf{K}_c\boldsymbol{\Phi}_a \\ \omega^2(\boldsymbol{\Omega}_s^2)^{-1}\boldsymbol{\Phi}_a^{\mathrm{T}}\mathbf{K}_c^{\mathrm{T}}\boldsymbol{\Phi}_s & -\dfrac{1}{\rho_0}\,(\boldsymbol{\Omega}_a^2 - \omega^2\mathbf{I}) - \omega^2\boldsymbol{\Phi}_a^{\mathrm{T}}\mathbf{K}_c^{\mathrm{T}}\boldsymbol{\Phi}_s(\boldsymbol{\Omega}_s^2)^{-1}\boldsymbol{\Phi}_s^{\mathrm{T}}\mathbf{K}_c\boldsymbol{\Phi}_a \end{bmatrix} \begin{Bmatrix} \bar{\mathbf{q}}_s \\ \mathbf{q}_a \end{Bmatrix} = \begin{Bmatrix} \mathbf{0} \\ \mathbf{0} \end{Bmatrix}. \tag{14}$$

The coupled modal vector $\bar{\boldsymbol{\Phi}} \in \mathbb{R}^{(n_s+n_a)\times(N_s+N_a)}$, resulting from the eigenproblem associated with Eq. (14) on $\{\bar{\mathbf{q}}_s \;\; \mathbf{q}_a\}^{\mathrm{T}}$, can be interpreted as the left eigenvector $\boldsymbol{\Phi}_L$ of the eigenproblem in Eq. (5) on $\{\mathbf{q}_s \;\; \mathbf{q}_a\}^{\mathrm{T}}$. The right eigenvector $\boldsymbol{\Phi}_R$ can be retrieved using Eq. (6).

Since the uncoupled bases $\boldsymbol{\Phi}_a$ and $\boldsymbol{\Phi}_s$ result from symmetric eigenproblems, solving Eq. (14) may seem less demanding when compared to the solution of Eqs. (4) and (5). However, the reduction on the computational effort is rather small; to accurately represent the coupled modes, it is necessary to retain a higher number of uncoupled modes. Nevertheless, the advantage of this method is the possibility of using dedicated software for each component uncoupled modal analysis.

Eventually, the structural and acoustic dofs $\{\mathbf{u} \;\; \mathbf{p}\}^{\mathrm{T}}$ can be projected using the modal base ($\boldsymbol{\Phi}_L$ and $\boldsymbol{\Phi}_R$) and the modal coordinate $\mathbf{q}$ using the following expansion:

$$\begin{Bmatrix} \mathbf{u} \\ \mathbf{p} \end{Bmatrix} = \sum_{r=1}^{N_s+N_a} q_r\{\boldsymbol{\Phi}_R\}_r = \boldsymbol{\Phi}_R\mathbf{q}. \tag{15}$$

Moreover, the left and right eigenvectors are normalized such that:

$$\boldsymbol{\Phi}_L^{\mathrm{T}}\begin{bmatrix} \mathbf{M}_s & \mathbf{0} \\ -\rho_0\mathbf{K}_c^{\mathrm{T}} & \mathbf{M}_a \end{bmatrix}\boldsymbol{\Phi}_R = \mathbf{I}, \tag{16}$$

$$\boldsymbol{\Phi}_L^{\mathrm{T}}\begin{bmatrix} \mathbf{K}_s & \mathbf{K}_c \\ \mathbf{0} & \mathbf{K}_a \end{bmatrix}\boldsymbol{\Phi}_R = \boldsymbol{\Omega}^2, \tag{17}$$

$$\boldsymbol{\Phi}_L^{\mathrm{T}}\begin{bmatrix} \mathbf{D}_s & \mathbf{0} \\ \mathbf{0} & \mathbf{D}_a \end{bmatrix}\boldsymbol{\Phi}_R = \boldsymbol{\Gamma}, \tag{18}$$

where $\mathbf{I}$, $\mathbf{\Omega}^2$ and $\mathbf{\Gamma} \in \mathbb{R}^{(N_s+N_a)\times(N_s+N_a)}$ are, respectively, the identity, the squared coupled natural frequencies and the modal damping matrices.

Applying the modal expansion described by Eq. (15) in Eq. (3) and pre-multiplying it by $\mathbf{\Phi}_L^{\mathrm{T}}$, Eq. (3) can be re-written as

$$\mathbf{\Phi}_L^{\mathrm{T}}\begin{bmatrix}\mathbf{K}_s & \mathbf{K}_c\\ \mathbf{0} & \mathbf{K}_a\end{bmatrix}\mathbf{\Phi}_R\mathbf{q}+\mathbf{\Phi}_L^{\mathrm{T}}\begin{bmatrix}\mathbf{D}_s & \mathbf{0}\\ \mathbf{0} & \mathbf{D}_a\end{bmatrix}\mathbf{\Phi}_R\dot{\mathbf{q}}+\mathbf{\Phi}_L^{\mathrm{T}}\begin{bmatrix}\mathbf{M}_s & \mathbf{0}\\ -\rho_0\mathbf{K}_c^{\mathrm{T}} & \mathbf{M}_a\end{bmatrix}\mathbf{\Phi}_R\ddot{\mathbf{q}}=\mathbf{\Phi}_L^{\mathrm{T}}\begin{Bmatrix}\mathbf{F}_s\\ \mathbf{F}_a\end{Bmatrix}. \tag{19}$$

Using the relations described by Eqs. (16)–(18), Eq. (19) can be described in a modal SS form:

$$\begin{Bmatrix}\dot{\mathbf{q}}\\ \ddot{\mathbf{q}}\end{Bmatrix}=\begin{bmatrix}\mathbf{0} & \mathbf{I}\\ -\mathbf{\Omega}^2 & -\mathbf{\Gamma}\end{bmatrix}\begin{Bmatrix}\mathbf{q}\\ \dot{\mathbf{q}}\end{Bmatrix}+\begin{bmatrix}\mathbf{0}\\ \mathbf{\Phi}_L^{\mathrm{T}}\mathbf{B}\end{bmatrix}\begin{Bmatrix}\mathbf{F}_{si}\\ \mathbf{F}_{ai}\end{Bmatrix}, \tag{20}$$

$$\begin{Bmatrix}\mathbf{u}_o\\ \mathbf{p}_o\end{Bmatrix}=[\mathbf{C}\mathbf{\Phi}_R\ \ \mathbf{0}]\begin{Bmatrix}\mathbf{q}\\ \dot{\mathbf{q}}\end{Bmatrix}, \tag{21}$$

where $\mathbf{B} \in \mathbb{R}^{(n_a+n_s)\times N_i}$ is a matrix with ones on the N_i desired input dofs and zeros everywhere else, $\mathbf{F}_{si} \in \mathbb{R}^{N_{si}\times 1}$ is the structural input load vector, $\mathbf{F}_{ai} \in \mathbb{R}^{N_{ai}\times 1}$ is the acoustic input load vector (with $N_{si}+N_{ai}=N_i$), $\mathbf{u}_o \in \mathbb{R}^{N_{so}\times 1}$ is the structural output vector, $\mathbf{p}_o \in \mathbb{R}^{N_{ao}\times 1}$ is the acoustic output vector (with $N_{so}+N_{ao}=N_o$) and $\mathbf{C} \in \mathbb{R}^{N_o\times(n_a+n_s)}$ is a matrix with ones on the N_o desired output dofs and zeros everywhere else. In this formulation, the role of $\mathbf{B}$ and $\mathbf{C}$ is to select, respectively, columns from $\mathbf{\Phi}_L^{\mathrm{T}}$ and rows from $\mathbf{\Phi}_R$ according to the desired input's and output's dofs.

Applying the aforementioned procedure, the original 24,192 dofs (23,196 unconstrained acoustic and 1026 unconstrained structural) have been reduced to an SS model with $2\times(N_s+N_a)$ dofs, related to the retained modal amplitudes $\mathbf{q}$ and their derivatives $\dot{\mathbf{q}}$, with force and volume velocity as inputs and displacement and pressure as outputs. The number of retained acoustic modal amplitudes is the same for all configurations, since the cavity compartments are not modified during the optimization procedure. Thus, $N_a=78$, i.e. the number of uncoupled acoustic modes with a natural frequency up to 400 Hz, which is adequate to represent the acoustic system in the frequency range of interest (0–200 Hz). In order to represent the structure (firewall) in the frequency range of interest, N_s may vary according to the number of modes occurring from 0 to 400 Hz. Table 2shows N_s for several firewall thicknesses. Considering the nominal 1.5 mm firewall, the total number of states is 214 ($2\times(78+29)$). Fewer states would lead to inaccuracies within the frequency of interest.

The validity of the reduced model is illustrated by comparing FRFs from the original model with the reduced model (Fig. 5). The system inputs are volume velocity applied in the EC (acoustic input) and force applied on the firewall (structural input), and the outputs are pressure measured at the PC (acoustic output) and displacement measured at the firewall (structural output). The good correlation between the reduced SS and the direct FE models validates the model reduction procedure.

2.2. Experimental validation

The FRFs derived from the SS model are compared with the FRFs measured on the cabin mock-up. The considered FRFs include structural and acoustic inputs and outputs. As depicted in Fig. 6(a), the structural excitation is performed with an LDS shaker (model V201/3), the force transducer is a PCB 208C04 and the accelerometers are PCB 352C67. Fig. 6(b) shows the LMS acoustic source (model E-LMFVVS) placed at the EC. The microphones used are B&K 4188. The vibro-acoustic system has been excited with white noise. The FRFs are measured with an Hv estimator, while input and output signals are filtered with Hanning windows.

Table 2
Retained structural modal amplitudes (N_s) for different firewall thickness

Firewall thickness (mm)	0.5	1.0	1.5	2.0	2.5	3.0	3.5	4.0	4.5
N_s	94	47	29	20	15	13	10	7	7

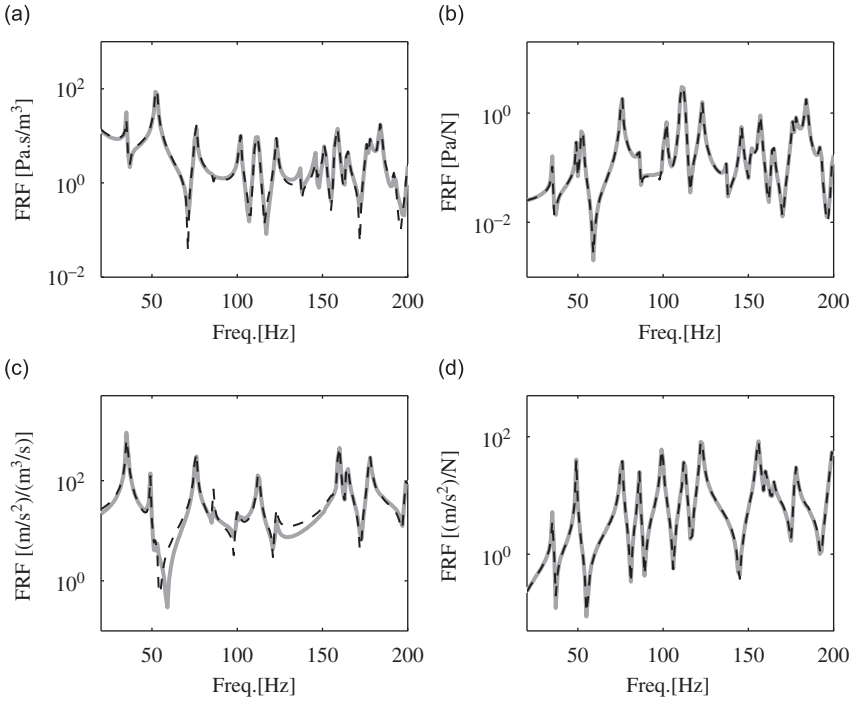

Fig. 5. Comparison between (- -) FE and (-) SS FRFs: (a) acoustic/acoustic, (b) acoustic/structural, (c) structural/acoustic and (d) structural/structural.

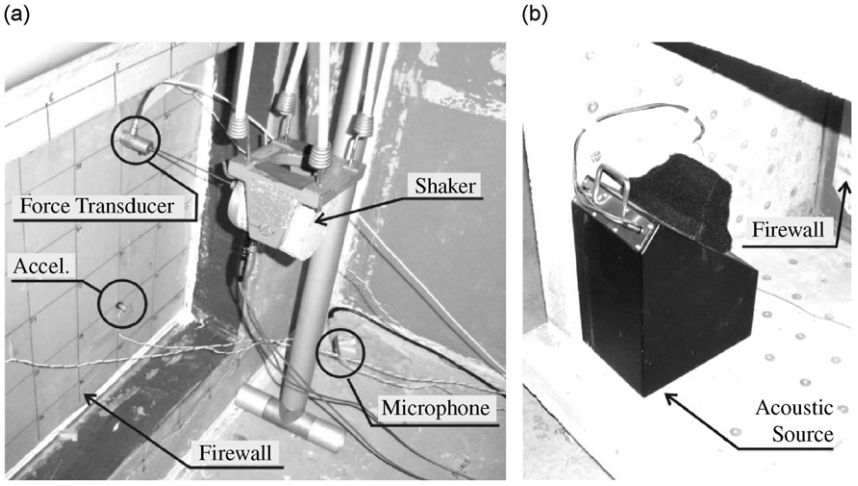

Fig. 6. Experimental setup: (a) view from the passenger compartment with shaker and sensors and (b) view from the engine compartment with sound source.

Fig. 7 shows a comparison between the experimental and the simulated (derived from the SS model) FRFs. The material properties adopted for this model (nominal case) are: speed of sound in the air $c_o = 344.7\,\mathrm{m/s}$, air density $\rho_0 = 1.185\,\mathrm{kg/m^3}$, firewall density (steel) $\rho_s = 7800\,\mathrm{kg/m^3}$ and elasticity modulus $E = 2.33\times 10^{11}$ Pa. A single modal damping ratio of 0.35% is applied in the SS model.

As can be seen, the resulting FRFs present a good agreement up to 150 Hz. Discrepancies above this frequency arise among others from the lack of accuracy in determining the exact place of the disturbance source, sensor/actuator pairs and microphones and from assuming the disturbance source as an ideal point

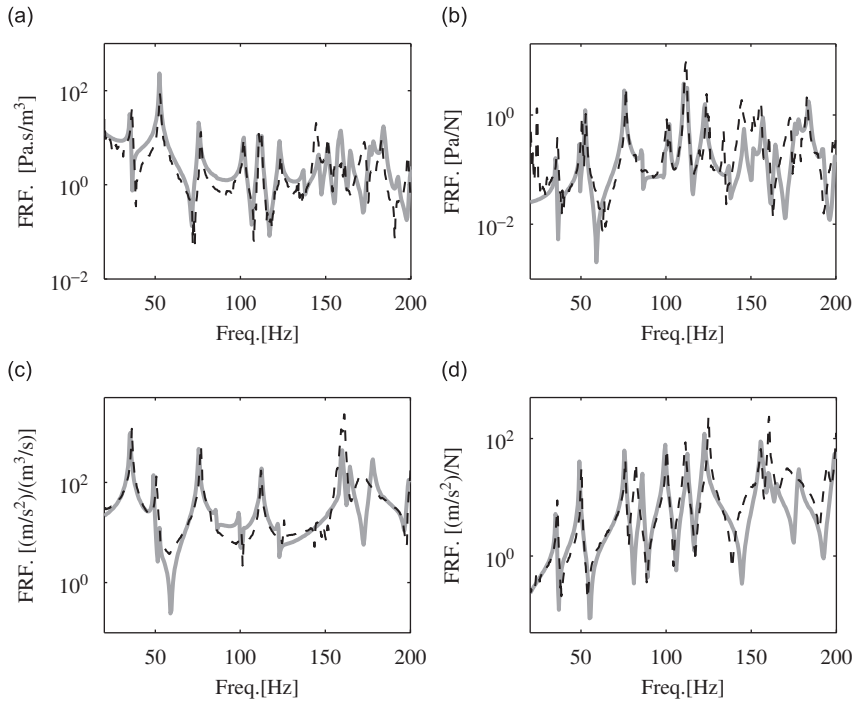

Fig. 7. Comparison between (-) SS and (- -) experimental FRFs: (a) acoustic/acoustic, (b) acoustic/structural, (c) structural/acoustic and (d) structural/structural.

source. Such mismatches are expected and reflect a limitation in the FE modeling rather than in the use of the reduced models in a closed-loop form, which is the focal point of this work.

2.3. Inclusion of sensor and actuators pairs (SAP) models

For ASAC simulations, the models must integrate not only structural and acoustic components but also sensors, actuators and the controller algorithm. The importance of including detailed information about the controller and the secondary paths is critical for an accurate assessment of the actual performance, since sensor and actuator dynamics can present frequency, phase and amplitude limitations. In order to cope with this strategy, the reduced model of the system, derived from the aforementioned methodology and described in a SS representation, is included in the control system design environment (Matlab/Simulink), where the interaction between the structure and the sensor/actuator can be taken into account.

In this case study, sensors and actuators are, respectively, accelerometers and inertial-shakers. Appropriate accelerometers are selected, for the frequency range of interest, such that the voltage signal generated by these devices can be considered proportional to the measured quantity. However, for the inertial-shakers, a more detailed model for the electro-mechanical coupling within the actuator and its interaction with the structure must be taken into account. The interaction between an electrodynamic shaker and the structure under test has been an issue since the very beginning of modal test methods (see e.g. Ref. [37,38]) and is still a subject of research [39–41].

Fig. 8 shows the electromechanical model of an inertial-shaker. The mechanical model (Fig. 8a) comprises the moving mass $m_i = 0.03\,\mathrm{kg}$, the suspension stiffness $k_i = 29.6\,\mathrm{N/m}$ and damping $c_i = 0.1\,\mathrm{N/(m/s)}$, the moving mass displacement u_i, the structure connecting point displacement u_s and the electro-magnetic force F_e. The electro-magnetic force is proportional to the current I in the circuit, $F_e = k_f I$, where $k_f = 4\,\mathrm{N/A}$ is the force–current constant.

The electrical model (Fig. 8b) includes the current I, the voltage input E, the circuit resistance $R = 4\,\Omega$, the inductance $L = 5\,\mu\mathrm{H}$ and the voltage generated by the moving coil E_{bemf}. The latter can be written in terms of

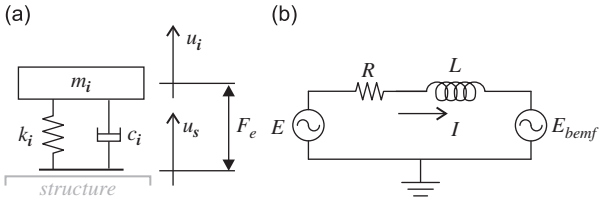

Fig. 8. Electromechanical model of an inertial shaker: (a) mechanical and (b) electrical model.

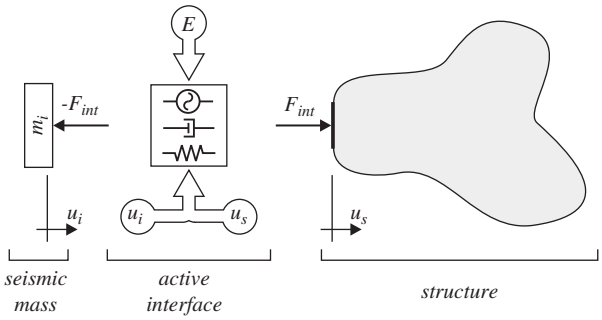

Fig. 9. Inertial-shaker active interface model.

the voltage constant $k_v = 4\,\mathrm{V/(m/s)}$ and the relative velocity between the structure connecting point and the moving mass, $E_{\mathrm{bemf}} = k_v(\dot{u}_s - \dot{u}_i)$. Eqs. (22) and (23) describe the dynamics of this coupled electro-mechanical system operating in voltage mode (ideal power amplifier).

$$RI + L\dot{I} + E_{\mathrm{bemf}} = E, \tag{22}$$

$$m_i\ddot{u}_i + c_i(\dot{u}_s - \dot{u}_i) + k_i(u_s - u_i) = F_e. \tag{23}$$

As proposed in Ref. [42], the inertial-shaker/structure interaction can be modeled as a moving mass and an active interface that includes the mechanical suspension and the electro-magnetic force (Fig. 9). Given the shaker model, the input voltage and the connecting point displacement, it is possible to estimate the force acting on the structure at the interface point (F_{int}). Substituting the current value I in Eq. (22) into Eq. (23) and neglecting the inductance L, since it is usually small [43], yields

$$F_{\mathrm{int}} = \frac{k_f}{R}E - \left[\frac{k_f}{R}k_v + c_i\right](\dot{u}_s - \dot{u}_i) - k_i(u_s - u_i). \tag{24}$$

Fig. 10(a) shows the structural FRF defined by u_s/F_{int} of the vibro-acoustic model and (b) a comparison between the idealized force input defined by $F_{id} = k_f E/R$, constant over frequency, the simulated load provided by an inertial-shaker, F_{int}, and the actual measured force, F_{exp}. It can be seen that, in the low-frequency range and in the vicinity of structural resonances, the force level drops, as a result of the shaker/structure interaction. The inclusion of the actuator model in the simulation allows the assessment of a phenomenon inherent to the use of such electrodynamic devices, i.e., the force drop-off around resonance frequencies. The drops in the excitation force can lead to errors in the experimental FRFs [40,41] but mainly, when the active control system is concerned, can result in overestimated authority and performance of the active solution [44].

The shaker model can be externally connected to any dof of the firewall, with the advantage of the SS model of the passive plant remaining unchanged (Fig. 11b). This is a useful structure for optimization as the SAP positions, i.e. the SS inputs, can be variables of the optimization procedure.

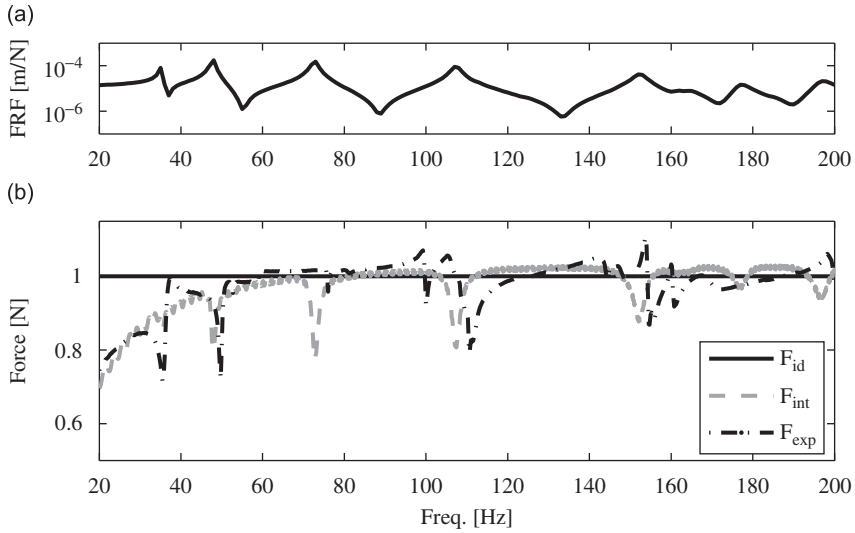

Fig. 10. (a) System driving point FRF and (b) input forces.

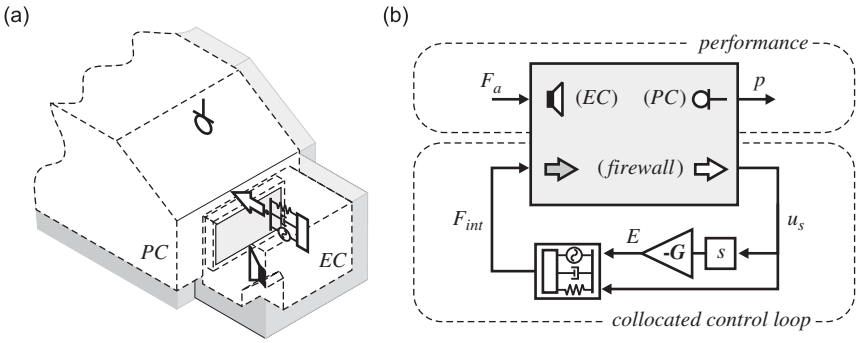

Fig. 11. Control scheme for the closed-loop vibro-acoustic system: (a) positions of sensors and actuators and (b) block diagram.

3. Concurrent mechatronic design of active systems

The main objective of the considered active control system is to minimize the noise transmitted from the EC to the PC. Among the parameters addressed during the design of an active system is the controller design more specifically, the definition of a control strategy, the selection and configuration of sensors and actuators, the parameters setting, etc. In a concurrent mechatronic approach, plant dynamic parameters could also be taken into account, aiming at an improved active system design.

Due to its relatively simple implementation, a time-invariant collocated velocity feedback is selected. In this application, the feedback gain on the structural SAP is optimized with respect to the pressure at the driver's ear, rather than the firewall vibration. This ASAC strategy is applicable when the acoustic source is transmitted into a cavity through a limited number of structural paths [1,45]. Fig. 11(a) shows a scheme of sensor and actuator positions and Fig. 11(b) shows a scheme of the adopted ASAC with the structural sensors and actuators involved in the control loop and the acoustic sensors and actuators related to the performance evaluation.

As a disturbance signal, an acoustic source in the EC that resembles engine noise is used (F_a in Fig. 11b). At constant speed, the characteristic frequency content of engine noise is a combination of the fundamental frequency (rotating speed), its harmonics and the background noise. During a run-up, these frequencies are swept, exciting a broad spectrum. After analyzing a series of time signals from real engine run-ups, the average amplitude of the disturbance signal was defined as depicted in Fig. 12.

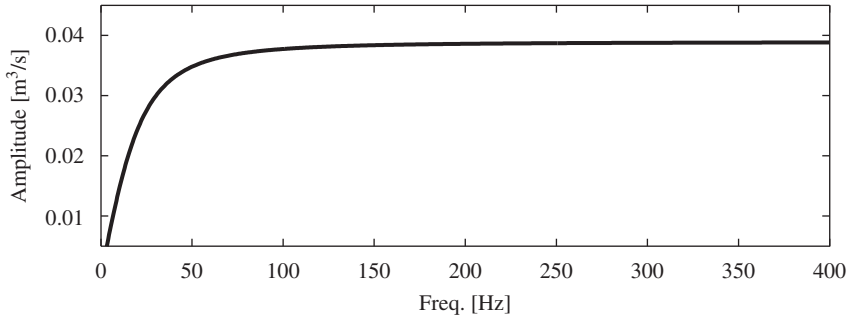

Fig. 12. Disturbance spectrum—acoustic input.

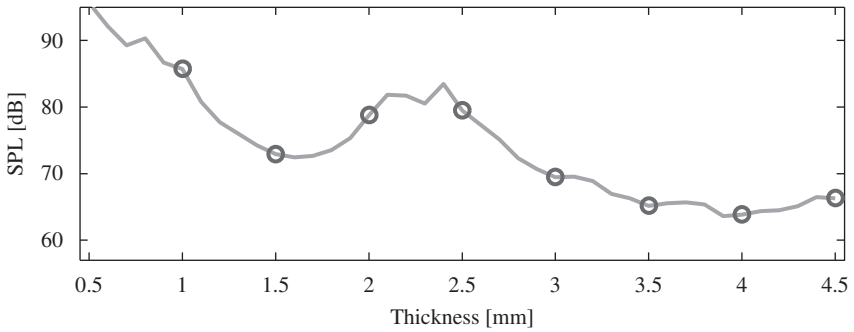

Fig. 13. Passive performance for several firewall thicknesses.

Since the control strategy is selected, the control design consists of determining the position of the SAP and the velocity feedback gain. The structural design parameter is the thickness of the firewall, as it directly affects the vibro-acoustic behavior of the system.

The metrics adopted to evaluate the design are the system performance, the control effort and the structural firewall mass. The performance of the system is defined as the sound pressure level (SPL), in dB, at the driver's ear position (Eq. (25)) and the control effort is defined as the applied control effort (COE), in V, (Eq. (26)).

$$\mathrm{SPL} = 20\log\left(\frac{p_{\mathrm{rms}}}{2\times 10^{-5}}\right), \tag{25}$$

$$\mathrm{COE} = G\dot{u}_{\mathrm{rms}}, \tag{26}$$

where p, in Pa, is the acoustic pressure, G, in V/(m/s), is the velocity feedback gain and $\dot{u}$, in m/s, is the structural velocity.

In a conventional design procedure, the structure is first optimized based on the passive performance and then, afterwards, an active control system is designed. Fig. 13 shows the passive performance for different firewall thicknesses (from 0.5 to 4.5 mm with a 0.1 mm step). Different performances occur due to the coupling between the structural and acoustic resonances. A good coupling between these resonances allows the noise at the EC to be transmitted through the firewall to the PC more efficiently, decreasing the performance, as occurs for instance for firewalls around 2.0 mm. On the other hand, the noise at EC will not be efficiently transmitted when the resonances and modes are not strongly coupled, increasing the performance, e.g. for the 1.5 mm firewall (Table 1). The markers in Fig. 13 represent the typical plate thicknesses readily available on the market, and therefore will be considered as the only feasible choices hereafter.

The presented optimization problem adopting a concurrent mechatronic design approach assumes that the controller is performed by a single collocated SAP. Therefore, the variables are the firewall thickness, the velocity feedback gain and the position of the SAP. This optimization problem deals with continuous variables, i.e. the feedback gain, and discrete variables, i.e. the firewall thickness (discrete values readily

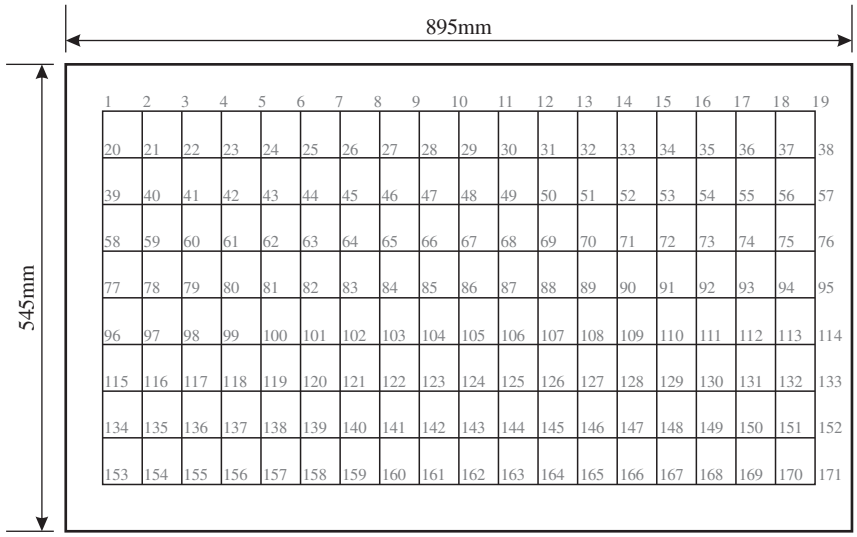

Fig. 14. Possible SAP positions on the firewall: the nodes on the firewall FE model.

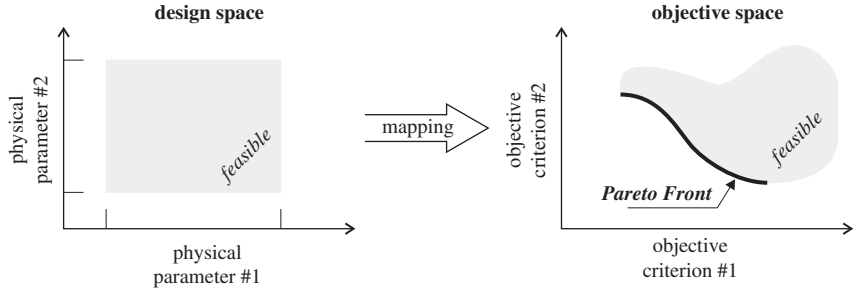

Fig. 15. Mapping from the design to the objective space.

available on the market) and the SAP position (node locations on the firewall FE model). In addition, this problem is non-convex and nonlinear. Since the model is of reduced size, an extensive search is performed for all possible configurations, comprising: all free nodes of the firewall as possible positions for the SAP (171 positions as indicated in Fig. 14), different thicknesses of the firewall (1.0, 1.5, 2.0 and 2.5 mm) and several feedback gains (from 0 to 10 kN/(m/s)).

Multi-objective optimization problems, usually, have conflicting objective functions. Therefore, the derivation of a single cost function as a weighted summation of those objectives [46] is not a trivial task since it may have a huge impact on the optimal design.

A more comprehensive strategy is to find the tradeoffs among several objectives. The Pareto plot represents the best obtainable compromises between all the conflicting objective functions [47]. This plot shows the feasible and infeasible design regions in the objective space. Fig. 15 shows the feasible region in the design space limited by the design constraints and its mapping to the objective space. The lower border between the feasible and infeasible regions in the objective space is the Pareto front. It contains the possible optimal combinations of the objectives. Objectives out of the border may lead to infeasible or suboptimal designs, i.e., for a solution belonging to this border it is not possible to improve one objective function without worsening another one [47]. Eventually, the solution derived by any single cost function is captured by the Pareto front. In this way, the designer can choose one single solution belonging to the Pareto front that suits better other design criteria.

Fig. 16 shows, for different firewall thicknesses, the Pareto plot considering performance and control effort. All feasible configurations, derived from an extensive search for various SAP locations and

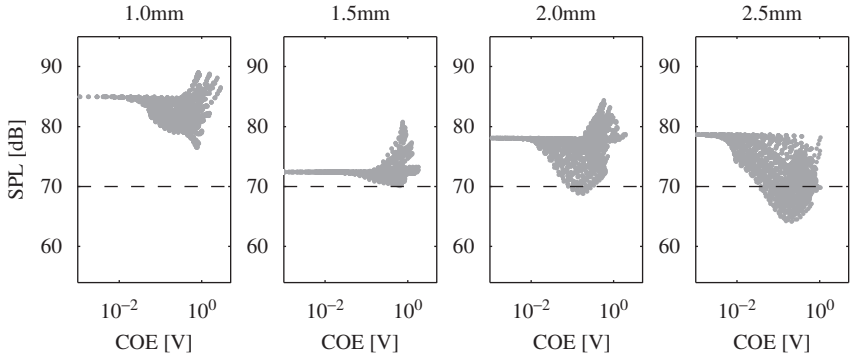

Fig. 16. Performance and control effort for different firewall thicknesses—Pareto plot.

feedback gains, are shown in this Pareto plot. The first conclusion that can be drawn is that the lightest option (1.0 mm) presents unsatisfactory passive and active performances. Therefore, considering performance and effort as design criteria, three configurations may be suitable: 1.5, 2.0 and 2.5 mm firewall. Among them, the lighter configuration, 1.5 mm, presents the best passive performance (72.4 dB as already indicated in Fig. 13).

According to a conventional design sequence, a natural choice would be to select the thinner firewall (1.5 mm), resulting in the lightest design and the best passive configuration. However, when the closed-loop performance is analyzed, the performance improvement of the lightest configuration is rather limited compared to the other configurations. For instance, requiring that the performance of the active system should be below 70.0 dB, the lightest configuration barely achieves this target (Fig. 16). Considering this target, the thicker configurations would achieve higher noise reduction, despite their lower passive performance. For a 70.0 dB target the lightest design is the 2.0 mm firewall. Moreover, it is possible to reach the same performance with less control effort by selecting the 2.5 mm firewall.

In summary, a conventional design sequence would lead to 1.5 mm firewall with the best possible closed-loop performance of 70.2 dB, while the concurrent mechatronic approach would lead to a 2.0 mm firewall with closed-loop performance up to 68.8 dB or even 2.5 mm achieving up to 64.1 dB. The concurrent mechatronic approach delivers better results than the conventional design sequence, since the system passive performance is not considered independently from the control dynamics.

Additionally, Fig. 16 shows that some SAP positions with a high-velocity feedback gain value, i.e. high effort values, can deteriorate the system performance compared with the passive performance. This phenomenon occurs because high-velocity feedback gains may clamp this position, modifying the dynamic behavior of the firewall, shifting natural frequencies and modes. Thus, the coupling between the acoustic and structural resonances can be amplified, deteriorating the system performance.

The system performance, according to the collocated SAP position, depends strongly on the firewall thickness. Fig. 17 shows the best achievable performance for each SAP position on the firewall (z and y directions) for different thicknesses. As mentioned before, this behavior can be explained by the fact that different thicknesses lead to differences in the structural resonance frequencies and, consequently, variations on the vibro-acoustic coupling. In this way, different vibro-acoustic modes may have a stronger contribution on the transmissibility process, resulting in distinct topologies for the optimum surfaces. As can be observed in Figs. 16 and 17, the same performance can be achieved by different configurations. These results justify the mechatronic design approach and illustrate the limits in the conventional design methodology for active vibro-acoustic applications.

Fig. 17 results from a priori derivation of reduced models for each firewall thickness. Each firewall thickness requires a reduced model. The required calculation time for deriving a reduced model depends a.o. on the modal density (see Table 2). Using a Pentium IV, with a processor of 1.4 GHz, the CPU time varied from 580 s for deriving the reduced model for the 2.5 mm firewall to 750 s for deriving the reduced model for the 1.0 mm firewall. The model reduction procedure is performed just once for each firewall thickness, since all possible

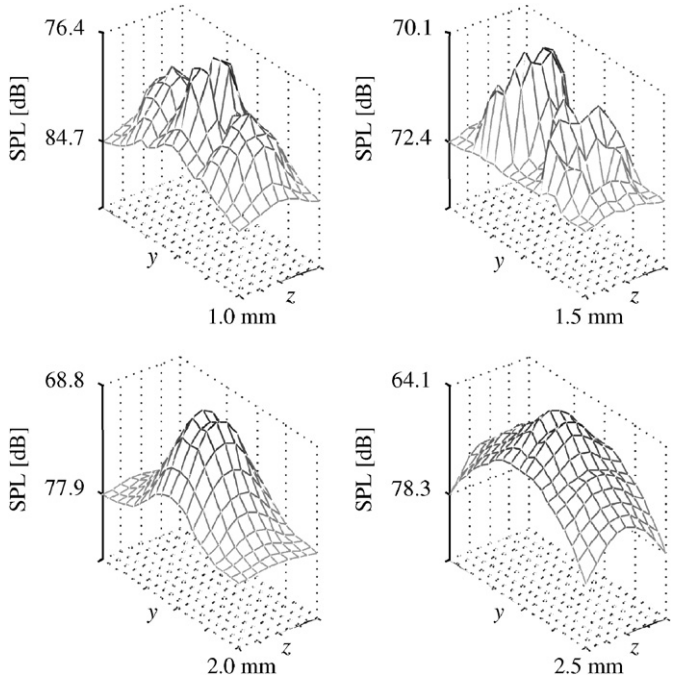

Fig. 17. Sound pressure level at each SAP position (with optimal gain) for different firewall thicknesses.

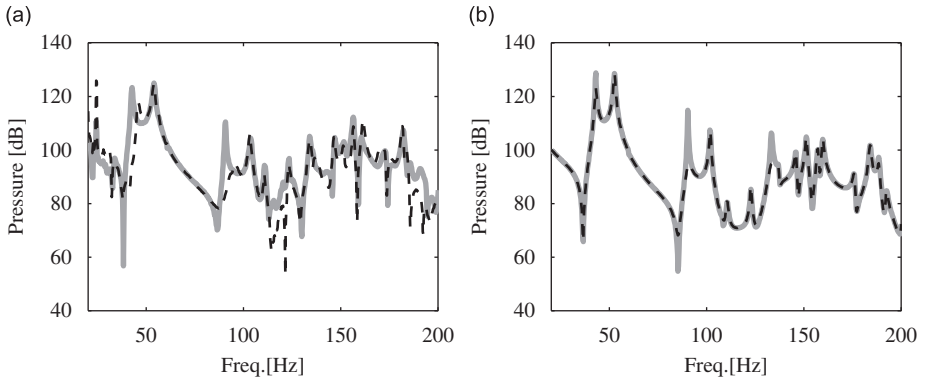

Fig. 18. Sound spectra at the driver's ear position for (-) passive system and (- -) suboptimal active system: (a) experimental and (b) simulation.

SAP positions are kept during the model reduction procedure. Once the reduced model is derived, the Pareto plot can be built finding the best gain for each possible SAP position. Using the same processor, this derivation took about 1500 s for each reduced model.

The numerical results have been verified experimentally by comparing the passive and active sound spectra at the driver's ear position for the 2.0 mm firewall. Fig. 18 shows the sub-optimal case, where the SAP is placed closer to the border (node 130 in Fig. 14) and the feedback gain is set to 466 V/(m/s). Fig. 19 shows the global optimal solution, with SAP at node 87 and feedback gain 466 V/(m/s). Table 3summarizes the SPL and the noise reduction for the passive, sub-optimal and optimal solutions depicted in Figs. 18 and 19. The good agreement between experiment and simulation corroborates the results presented and emphasizes the benefits of the proposed concurrent mechatronic approach.

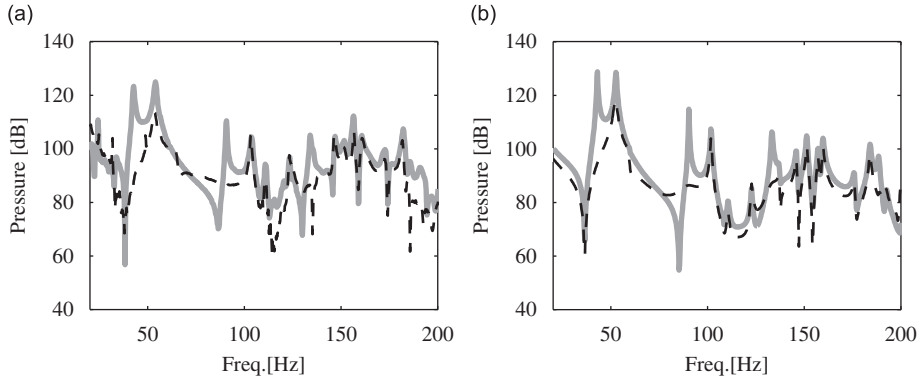

Fig. 19. Sound spectra at the driver's ear position for (-) passive system and (- -) optimal active system: (a) experimental and (b) simulation.

Table 3
Experimental and simulated SPL at the driver's ear for passive, sub-optimal and optimal solutions

Solution	Experiments		Simulation	
	SPL (dB)	Reduction (dB)	SPL (dB)	Reduction (dB)
Passive	76.7	–	78.0	–
Sub-optimal	75.8	0.9	76.6	1.4
Optimal	67.9	8.8	68.8	9.2

4. Conclusions and future work

A concurrent mechatronic approach for ASAC, considering a fully coupled vibro-acoustic system with SAP models, has been presented. This general approach allows the inclusion of any kind of controller that uses structural or acoustic sensors and actuators. The modeling procedure was validated by correlating the direct FE and the reduced SS models. Eventually, the vibro-acoustic model reduction procedure was experimentally validated for a system that resembles a passenger vehicle interior.

The benefits of this approach have been exploited in some investigations considering structural and control parameters as the firewall thickness, the velocity feedback gain and the position of the SAP. The first conclusion that can be outlined is that optimal passive performance systems may have inferior closed-loop performance. Consequently, an optimal design can only be achieved when considering structure and control concurrently.

Considering that an ASAC modeling procedure is a multi-disciplinary assignment, distinct objectives arise from these disciplines. Capturing the design tradeoffs, using for instance the Pareto front, can assist the designer to gain better insights into the problem.

Comparisons between experimental and simulation results for the passive, sub-optimal and optimal solutions showed good agreement confirming the benefits of the proposed concurrent mechatronic approach for ASAC design.

Given the potential of piezoelectric materials for active control purposes, a next step in this study will be the inclusion of distributed sensors and actuators in the methodology. As optimization variables, not only the placements and the control gains but also the shape of the piezo-patches may then be considered.

Acknowledgments

The research of Leopoldo P.R. de Oliveira is supported in the framework of a bilateral agreement between KU Leuven and University of São Paulo. The support for the research of Maíra M. da Silva is provided by

CAPES, Brazilian Foundation Coordination for the Improvement of Higher Education Personnel. The research presented in this paper was performed as part of the FP6-Integrated Project InMAR, "Intelligent Materials for Active Noise Reduction". We are also grateful to LMS International for the technical support and encouragement.

References

[1] S.J. Elliott, Active control of structure-borne noise, *Journal of Sound and Vibration* 177 (1994) 651–673.
[2] S.J. Elliott, I.M. Stothers, P.A. Nelson, A.M. McDonald, D.C. Quinn, T. Saunders, The active control of engine noise inside cars, *InterNoise* 88, Avignon, France, September 1988, pp. 987–990.
[3] W. Dehandschutter, P. Sas, Active control of structure-borne road noise using vibration actuators, *Journal of Vibration and Acoustics* 120 (2) (1998) 517–523.
[4] C. Park, C. Fuller, M. Kidner, Evaluation and demonstration of advanced active noise control in a passenger automobile, *Proceedings of ACTIVE 2002*, Southampton, UK, July 15–17, 2002, pp. 275–284.
[5] C.G. Park, C. Fuller, J.P. Carneal, V. Collin, J.T. Long, R.E. Powell, J.L. Schmidt, On-road demonstration of noise control in a passenger automobile—part 2, *Proceedings of ACTIVE 04*, Williamsburg, Virginia, September 20–22, 2004, pp. 1–12.
[6] A. Gonzaleza, M. Ferrera, M. de Diegoa, G. Pineroa, J.J. Garcia-Bonito, Sound quality of low-frequency and car engine noises after active noise control, *Journal of Sound and Vibration* 265 (2003) 663–679.
[7] K. Henrioulle, P. Sas, Experimental validation of a collocated PVDF volume velocity sensor/actuator pair, *Journal of Sound and Vibration* 265 (2003) 489–506.
[8] S.J. Elliott, P. Gardonio, T.C. Sors, M.J. Brennan, Active vibroacoustic control with multiple local feedback loops, *Journal of the Acoustical Society of America* 111 (2002) 908–915.
[9] L.P.R. Oliveira, B. Stallaert, W. Desmet, J. Swevers, P. Sas, Optimisation strategies for decentralized ASAC, *Proceedings of Forum Acusticum 2005*, Budapest, 2005, pp. 875–880.
[10] A. Preumont, *Vibration Control of Active Structures: An Introduction*, second ed., Kluwer Academic Publishers, Dordrecht, 2002.
[11] O.N. Baumann, W.P. Engels, S.J. Elliott, A comparison of centralised and decentralised control for the reduction of kinetic energy and radiated sound power, *Proceedings of ACTIVE 04*, Williamsburg, Virginia, September 20–22, 2004, pp. 1–11.
[12] P. de Fonseca, P. Sas, H. Van Brussel, A comparative study of methods for optimizing sensor and actuator locations in active control applications, *Journal of Sound and Vibration* 221 (1999) 651–679.
[13] W. Liu, Z. Hou, M.A. Demetriou, A computational scheme for the optimal sensor/actuator placement of flexible structures using spatial H2 measures, *Mechanical Systems and Signal Processing* 20 (2006) 881–895.
[14] H. Van der Auweraer, K. Janssens, L. de Oliveira, M. da Silva, W. Desmet, Virtual prototyping for sound quality design of automobiles, *Sound and Vibration* April (2007) 26–30.
[15] J. Van Amerongen, P. Breedveld, Modelling of physical systems for the design and control of mechatronic systems, *Annual Reviews in Control* 27 (2003) 87–117.
[16] H. Van Brussel, P. Sas, I. Németh, P. De Fonseca, P. Van den Braembussche, Towards a mechatronic compiler, *IEEE/ASME Transactions on Mechatronics* 6 (1) (2001) 90–105.
[17] Z. Xianmin, L. Jianwei, S. Yunwen, Simultaneous optimal structure and control design of flexible linkage mechanism for noise attenuation, *Journal of Sound and Vibration* 299 (2007) 1124–1133.
[18] J.A. Giordano, G.H. Koopmann, G.H., State-space boundary element-finite element coupling for fluid–structure interaction analysis, *Journal of the Acoustical Society of America* 98 (1995) 363–372.
[19] K.A. Cunefare, S. De Rosa, S., An improved state-space method for coupled fluid–structure interaction analysis, *Journal of the Acoustical Society of America* 105 (1999) 206–210.
[20] S. Li, A state-space coupling method for fluid–structure interaction analysis of plates, *Journal of the Acoustical Society of America* 118 (2005) 800–805.
[21] L.P.R. Oliveira, A. Deraemaeker, J. Mohring, H. Van der Auweraer, P. Sas, W. Desmet, A CAE modeling approach for the analysis of vibroacoustic systems with distributed ASAC control, *Proceedings of ISMA2006*, Leuven, Belgium, September 2006, 2006, pp. 321–336.
[22] J.I. Mohammed, S.J. Elliott, Active control of fully coupled structural–acoustic systems, *Proceeding of Inter-Noise 2005*, Rio de Janeiro, Brazil, 2005, pp. 1–10.
[23] W. Desmet, B. Pluymers, P. Sas, Vibro-acoustic analysis procedures for the evaluation of the sound insulation characteristics of agricultural machinery cabins, *Journal of Sound and Vibration* 266 (2003) 407–441.
[24] P. Sas, C. Bao, F. Augusztinovicz, W. Desmet, Active control of sound transmission through a double panel partition, *Journal of Sound and Vibration* 180 (4) (1995) 609–625.
[25] G. Pan, D.A. Bies, The effect of fluid structure coupling on the sound waves in an enclosure: theoretical part, *Journal of the Acoustical Society of America* 2 (1987) 691–706.
[26] G.C. Everstine, A symmetric potential formulation for fluid–structure interactions, *Journal of Sound and Vibration* 79 (1981) 157–160.
[27] L.G. Olson, K.J. Bathe, Analysis of fluid–structure interactions: a direct symmetric coupled formulation based on the fluid velocity potential, *Computers & Structures* 21 (1985) 21–32.

[28] W. Desmet, D. Vandepitte, Finite element method in acoustics, *Seminar on Advanced Techniques in Applied and Numerical Acoustics—ISAAC17*, Leuven, Belgium, September 2006, pp. 1–48.
[29] J.P. Coyette, Y. Dubois-Pèlerin, An efficient coupling procedure for handling large size interior structural–acoustic problems, *Proceedings of ISMA-19*, Leuven, Belgium, September 1994, pp. 729–738.
[30] MSC. Nastran Reference Manual, MSC Software, USA, 2004.
[31] G.C. Everstine, Structural acoustic analogies for scalar field problems, *International Journal of Numerical Methods in Engineering* 17 (3) (1981) 471–476.
[32] G.C. Everstine, Finite element formulations of structural acoustics problems, *Computers and Structures* 65 (1997) 307–321.
[33] S. De Rosa, G. Pezzullo, L. Lecce, F. Marulo, Structural acoustic calculations in the low frequency range, *AIAA Journal of Aircraft* 31 (6) (1994) 1387–1394.
[34] W. Desmet, A Wave Based Prediction Technique for Coupled Vibro-acoustic Analysis, PhD Thesis, Mechanical Engineering Department, Katholieke Universiteit Leuven, PMA, 1998.
[35] J. Luo, H.C. Gea, Modal sensitivity analysis of coupled acoustic–structural systems, *Journal of Vibration and Acoustics* 119 (1997) 545–550.
[36] Sysnoise rev. 5.5 User's Manual, LMS International, Leuven, Belgium, 2000.
[37] K. Unholtz, *Vibration Testing Machines—Shock and Vibration Handbook*, vol. 2, first ed., McGraw-Hill Book Co., New York, 1961, pp. 25.1–25.74.
[38] G.R. Tomlinson, Force distortion in resonance testing of structures with electrodynamic vibration exciters, *Journal of Sound and Vibration* 63 (1979) 337–350.
[39] K.G. McConnell, P.S. Varoto, *Vibration Testing: Theory and Practice*, Wiley, NY, EUA, 1995.
[40] T. Olbrechts, P. Sas, D. Vandepitte, FRF measurement errors caused by the use of inertia mass shakers, *Proceedings of the 15 International Modal Analysis Conference, IMAC*, 1997, pp. 188–194.
[41] P.S. Varoto, L.P.R. Oliveira, On the force drop-off phenomenon in shaker testing in experimental modal analysis, *Shock and Vibration* 9 (2002) 165–175.
[42] S. Herold, H. Atzrodt, D. Mayer, M. Thomaier, Integration of different approaches to simulate active structures for automotive applications, *Proceedings of Forum Acusticum 2005*, Budapest, Hungary, pp. 909–914.
[43] N.M.M. Maia, J.M.M. Silva, *Theoretical and Experimental Modal Analysis*, Wiley, New York, 1997.
[44] L.P.R. Oliveira, P.S. Varoto, P. Sas, W. Desmet, A state-space approach for ASAC simulation, *Proceedings of the XII International Symposium on Dynamic Problems of Mechanics (DINAME 2007)*, 2007, pp. 1–10.
[45] P.A. Nelson, S.J. Elliot, *Active Control of Sound*, Academic Press, 1992.
[46] S. De Rosa, A. Sollo, F. Franco, K. A. Cunefare, Structural–acoustic optimisation of a partial fuselage with a standard finite element code, *7th AIAA/CEAS Aeroacoustics Conference and Exhibit*, Maastricht, Netherlands, May 28–30, 2001; Collection of Technical Papers. vol. 1 (A01-30800 07-71) AIAA-2001-2114.
[47] M. Gobbi, F. Levi, G. Mastinu, Multi-objective stochastic optimisation of the suspension system of road vehicles, *Journal of Sound and Vibration* 298 (2006) 1055–1072.